Solving nonequilibrium dynamical mean-field theory using matrix product states

F. Alexander Wolf,[1] Ian P. McCulloch,[2] and Ulrich Schollwöck[1]

[1]*Theoretical Nanophysics, Arnold Sommerfeld Center for Theoretical Physics, LMU Munich, Theresienstrasse 37, 80333 München, Germany*
[2]*Centre for Engineered Quantum Systems, School of Physical Sciences, The University of Queensland, Brisbane, Queensland 4072, Australia*

We solve nonequilibrium dynamical mean-field theory (DMFT) using matrix product states (MPS). This allows us to treat much larger bath sizes and by that reach substantially longer times (factor $\sim$ 2–3) than with exact diagonalization. We show that the star geometry of the underlying impurity problem can have substantially better entanglement properties than the previously favored chain geometry. This has immense consequences for the efficiency of an MPS-based description of general impurity problems: in the case of equilibrium DMFT, it leads to an orders-of-magnitude speedup. We introduce an approximation for the two-time hybridization function that uses time-translational invariance, which can be observed after a certain relaxation time after a quench to a time-independent Hamiltonian.

I. INTRODUCTION

The dynamical mean-field theory (DMFT) [1–4] is among the most successful methods to study strongly correlated electron systems in higher dimensions. DMFT maps a lattice model such as the Hubbard model onto an effective impurity model, which can be solved at considerably lower numerical cost. The resulting approximation becomes exact in the limit of infinite dimensions [1], and is usually good for three-dimensional systems. In the past years, the nonequilbrium formulation of DMFT (NEQDMFT) [5–7], which generalizes DMFT to the Keldysh formalism, has become widely employed.

To advance DMFT in the nonequilibrium regime, one still needs efficient methods to solve the real-time dynamics of the effective underlying impurity model far from equilibrium. Impurity solvers that have been used so far include real-time continuous-time quantum Monte Carlo [8], which is numerically exact, but restricted to short times due to the *phase* problem. Furthermore, there are strong- [9] and weak-coupling expansions [10–12], which are restricted to certain parameter regimes, and a formulation of NEQDMFT, that is able treat the steady-state case efficiently [13]. Recently, a Hamiltonian-based impurity solver scheme has been developed, which maps the DMFT impurity model onto a single-impurity Anderson model (SIAM) with a finite number of bath orbitals [14]. This could be solved with exact diagonalization in all parameter regimes. While the representation of the DMFT bath with a SIAM can be made exact for small times, it requires an increasing number of bath orbitals to reach longer times [14,15]. The exponential scaling of the Hilbert space dimension as a function of the number of bath orbitals therefore prohibits to acquire the dynamics at long time scales.

Various approaches exist to overcome this limitation in the representation of the wave function. These notably include (time-dependent) DMRG [16,17], which is based on a matrix product state (MPS) representation, and tensor-network representations of many-fermion states [18,19]. Recently, the so-called multiconfiguration time-dependent Hartree method [20] was applied to solve the Hamiltonian representation of DMFT. In this paper, we study the application of MPS-based methods to it.

The paper is organized as follows. In Sec. II, we briefly give the basic definitions of nonequilibrium DMFT. Motivated by

the fact that the mapping on a SIAM in NEQDMFT is simple if the SIAM is in the star geometry, while it is unsolved for the chain geometry, in Sec. III, we compare the entanglement properties for the two cases. As these should not depend on whether Hamiltonian parameters are time dependent or not, we do this for the equilibrium case. Unexpectedly, we find that the star geometry can have much better entanglement properties than the chain geometry. In Sec. IV, we numerically solve the NEQDMFT and analyze the computational resources needed to do so. In Sec. V, we propose a specific extrapolation of the hybridization function that uses time-translational invariance, which is reestablished after a certain relaxation phase after a quench to a time-independent Hamiltonian. In Sec. VI, we conclude the paper.

II. BASICS OF NONEQUILBRIUM DMFT

We aim to describe the real-time evolution of a lattice quantum many-body system such as the single-band Hubbard model

$$H_{\text{Hub}}(t) = -v(t) \sum_{ij\sigma} c_{i\sigma}^\dagger c_{j\sigma} + U(t) \sum_i \left(n_{i\uparrow} - \frac{1}{2} \right) \left(n_{i\downarrow} - \frac{1}{2} \right), \quad (1)$$

where $c_{i\sigma}^\dagger$ ($c_{i\sigma}$) creates (annihilates) an electron with spin σ on site i of the crystal lattice, $n_{i\sigma}$ is the spin-resolved density, $v(t)$ is the hopping energy, and $U(t)$ is the local interaction energy.

The central task of nonequilibrium DMFT based on the Keldysh formalism [21] is to compute the local contour-ordered Green's function

$$G_\sigma(t,t') = -i \langle T_{\mathcal{C}} c_\sigma(t) c_\sigma^\dagger(t') \rangle_{S_{\text{loc}}} \quad (2)$$

of an effective single-site impurity model that approximates the lattice model (1). The time arguments of contour-ordered functions lie on the L-shaped Keldysh contour $\mathcal{C}$, and $\langle T_{\mathcal{C}} \ldots \rangle_{S_{\text{loc}}} \equiv \text{Tr}[T_{\mathcal{C}} e^{S_{\text{loc}}} \ldots]/\text{Tr}[T_{\mathcal{C}} e^{S_{\text{loc}}}]$ denotes the contour-ordered expectation value [7]. For real-time arguments as studied in this paper, though, different orderings on the L-shaped contour simply lead to the familiar definitions of retarded and advanced Green's functions. The action S_{loc} of

the effective model is given by ($\hbar \equiv 1$)

$$S_{\text{loc}} = -i \int_{\mathcal{C}} dt \left(U(t) \left[n_{\uparrow}(t) - \frac{1}{2} \right] \left[n_{\downarrow}(t) - \frac{1}{2} \right] \right.$$
$$\left. - \mu \sum_{\sigma} n_{\sigma}(t) \right) - i \int_{\mathcal{C}} \int_{\mathcal{C}} dt \, dt'$$
$$\times \sum_{\sigma} c_{\sigma}^{\dagger}(t) \Lambda_{\sigma}(t,t') c_{\sigma}(t'), \quad (3)$$

where the first part describes the local energies associated with the impurity (μ denotes the chemical potential), and the second part describes the hybridization of the impurity with a bath of noninteracting fermions. This Gaussian bath is integrated out and by that gives rise to the two-time hybridization function $\Lambda_{\sigma}(t,t')$. $\Lambda_{\sigma}(t,t')$ must be determined self-consistently such that the resulting self-energy of the effective impurity model equals the local self-energy of the lattice model. In the simplest case of a Bethe lattice with nearest-neighbor hopping in the limit of infinite coordination number Z, this requirement leads to a self-consistency relation of closed form [22]

$$\Lambda_{\sigma}(t,t') = v(t) G_{\sigma}(t,t') v(t'), \quad (4)$$

where the hopping matrix elements in Eq. (1) have been rescaled according to $v(t) \rightarrow v(t)/\sqrt{Z}$ [1].

A. Hamiltonian representation

The DMFT action S_{loc} in Eq. (3) can also be represented by a time-dependent Anderson model (SIAM) [14]

$$H(t) = H_{\text{imp}}(t) + H_{\text{bath}}(t) + H_{\text{hyb}}(t),$$

$$H_{\text{imp}}(t) = U(t) \left(n_{0\uparrow} - \frac{1}{2} \right) \left(n_{0\downarrow} - \frac{1}{2} \right) - \mu \sum_{\sigma} n_{0\sigma},$$

$$\qquad\qquad (5)$$

$$H_{\text{bath}}(t) = \sum_{l=1}^{L_b} \sum_{\sigma} \epsilon_{l\sigma} c_{l\sigma}^{\dagger} c_{l\sigma},$$

$$H_{\text{hyb}}(t) = \sum_{l=1}^{L_b} \sum_{\sigma} (V_{l\sigma}(t) c_{0\sigma}^{\dagger} c_{l\sigma} + \text{H.c.}),$$

where the impurity at site 0 is coupled with hopping energies $V_{l\sigma}(t)$ in a star geometry to L_b noninteracting bath orbitals at potentials $\epsilon_{l\sigma}$, which can be chosen to be time independent [14]. The hybridization function of a SIAM is

$$\Lambda_{\sigma}^{\text{SIAM}}(t,t') = \sum_{l=1}^{L_b} V_{l\sigma}(t) g(\epsilon_{l\sigma},t,t') V_{l\sigma}(t')^*, \quad (6)$$

where

$$g(\epsilon_{l\sigma},t,t') = -i[\theta_{\mathcal{C}}(t,t') - f(\epsilon_{l\sigma})] e^{-i\epsilon_{l\sigma}(t-t')} \quad (7)$$

is the Green's function of an isolated bath orbital, $f(\epsilon) = 1/(e^{\beta\epsilon} + 1)$ denotes the Fermi distribution, and $\theta_{\mathcal{C}}(t,t')$ is the contour step function

$$\theta_C(t,t') = \begin{cases} 1 & \text{for} \quad t \geqslant_C t', \\ 0 & \text{else.} \end{cases} \quad (8)$$

B. How to obtain the Hamiltonian parameters?

It remains to solve the following problem: Given the hybridization function $\Lambda_{\sigma}(t,t') = v(t) G_{\sigma}(t,t') v(t')$, obtained from the self-consistency condition (4), one needs to determine the Hamiltonian parameters of the SIAM (5) that generate this hybridization function $\Lambda_{\sigma}^{\text{SIAM}}(t,t') = \Lambda_{\sigma}(t,t')$ via Eq. (6).

To achieve this [14,23], two distinct baths have to be introduced: the *first* bath $\Lambda_{\sigma}^{\text{SIAM},-}$ describes initial correlations in the system, whereas the *second* bath $\Lambda_{\sigma}^{\text{SIAM},+}$ describes the dynamic buildup of correlations. The parameters $V_{l\sigma}(t)$ and $\epsilon_{l\sigma}$ that generate the *first* bath can be directly expressed using the bath spectral function that corresponds to $\Lambda(t,t')$. The parameters for the *second* bath have to be constructed using a matrix factorization of $\Lambda(t,t')$. As in this work, for simplicity, only time evolutions from uncorrelated initial states are considered, $\Lambda_{\sigma}^{\text{SIAM},-}(t,t') \equiv 0$, and we only recapitulate the construction of the *second* bath $\Lambda_{\sigma}^{\text{SIAM},+} \equiv \Lambda_{\sigma}^{\text{SIAM}}$.

In this case, it will be sufficient to consider Green's functions and the hybridization function only for real-time arguments. For real times, rewriting the contour-ordered Green's function (2) using the *greater* and *lesser* Green's function and introducing an analogous definition for the hybridization function leads to

$$G(t,t') = \theta_C(t,t') G_{\sigma}^{>}(t,t') + \theta_C(t',t) G_{\sigma}^{<}(t,t'), \quad (9)$$

$$\Lambda_{\sigma}(t,t') = \theta_C(t,t') \Lambda_{\sigma}^{>}(t,t') + \theta_C(t',t) \Lambda_{\sigma}^{<}(t,t'), \quad (10)$$

where

$$G^{>}(t,t') = -i \langle c(t) c^{\dagger}(t') \rangle_{S_{\text{loc}}}, \quad (11\text{a})$$

$$G^{<}(t,t') = i \langle c^{\dagger}(t') c(t) \rangle_{S_{\text{loc}}}. \quad (11\text{b})$$

This allows us to rewrite the self-consistency (4) as

$$\Lambda_{\sigma}^{\gtrless}(t,t') = v(t) G_{\sigma}^{\gtrless}(t,t') v(t'). \quad (12)$$

Independent of that, $\Lambda^{\text{SIAM}}(t,t')$ in (6) can be simplified due to a freedom in choice for the bath potentials $\epsilon_{l\sigma}$, which are chosen to have different initial and final constant values [14]. Choosing $\epsilon_{l\sigma} = 0$ for the final value cancels the oscillatory term $e^{-i\epsilon_{l\sigma}(t-t')}$ in Eq. (7). Considering occupied sites with initial potential energy $\epsilon_{l\sigma} < 0$ at $T = 0$, one has $g(\epsilon_{l\sigma},t,t') = -i[\theta_{\mathcal{C}}(t,t') - 1] = i\theta_{\mathcal{C}}(t',t)$, whereas for unoccupied orbitals with initial $\epsilon_{l\sigma} > 0$ one has $g(\epsilon_{l\sigma},t,t') = -i\theta_{\mathcal{C}}(t,t')$.

Rewriting Eq. (6) with this choice [14] for the potential energies gives

$$\Lambda_{\sigma}^{\text{SIAM}}(t,t') = i\theta_{\mathcal{C}}(t',t) \sum_{l \text{ occ.}} V_{l\sigma}(t) V_{l\sigma}(t')^*$$
$$- i\theta_{\mathcal{C}}(t,t') \sum_{l \text{ unocc.}} V_{l\sigma}(t) V_{l\sigma}(t')^*. \quad (13)$$

Comparison with Eq. (10) then allows us to rewrite the self-consistency for the *greater* and *lesser* hybridization functions

as

$$\Lambda_\sigma^<(t,t') = i \sum_{l=1}^{L_b/2} V_{l\sigma}(t) V_{l\sigma}(t')^*, \tag{14a}$$

$$\Lambda_\sigma^>(t,t') = -i \sum_{l=L_b/2+1}^{L_b} V_{l\sigma}(t) V_{l\sigma}(t')^*, \tag{14b}$$

where we assumed the first half of bath orbitals to be occupied, and the second half to be unoccupied. If one can solve these equations for the couplings $V_{l\sigma}(t)$, the construction of the appropriate SIAM is completed. In the limit $L_b \to \infty$, one can always find functions $V_{l\sigma}(t)$ that allow us to represent the two-time functions $\Lambda_\sigma^{\gtrless}(t,t')$ via Eq. (14). For a finite number of bath sites, this is not guaranteed, and approximation methods have to be used. The method of choice [14] is a Cholesky factorization of the matrices $\pm i\Lambda_\sigma^{\gtrless}(t,t')$ (the two-time function becomes a matrix with two discrete indices upon time discretization) combined with an optimization procedure [14]. Both are standard numerical routines and straightforwardly give the Hamiltonian parameters $V_{l\sigma}(t)$.

C. Equilibrium case

To make the connection with exisiting treatments of DMFT calculations with DMRG [24–32], we give the equations for the equilibrium case. In equilibrium, all relevant two-time functions are time-translationally invariant and become functions of effectively one time argument, e.g.,

$$G_\sigma^R(t,t') = -i\theta(t-t')[G^>(t,t') - G^<(t,t')]$$
$$\equiv G_\sigma^R(t-t') \tag{15}$$

for the retarded component of the Green's function. One can therefore consider the corresponding one-argument Fourier (Laplace) transformed representation of such functions, e.g., $G_\sigma(\omega) = \int dt\, e^{i\omega t} G_\sigma^R(t,0)$, which is analytic in the upper half complex plane $\{\omega | \mathrm{Re}(\omega) > 0; \omega \in \mathbb{C}\}$, or $\Lambda_\sigma(\omega) = \int dt\, e^{i\omega t} \Lambda_\sigma(t,0)$. The analogous self-consistency condition to Eq. (4) then is

$$\Lambda_\sigma(\omega) = v^2 G_\sigma(\omega). \tag{16}$$

The Fourier transform of the hybridization function of the SIAM Eq. (6) is

$$\Lambda_\sigma^{\mathrm{SIAM}}(\omega) = \sum_{l=1}^{L_b} \frac{|V_{l\sigma}|^2}{\omega - \epsilon_{l\sigma}}, \tag{17}$$

with now time-independent hybridization couplings $V_{l\sigma}$.

When solving the self-consistency condition (16) with the help of a Fourier transform of $G_\sigma^R(t,0)$, one has to know $G_\sigma^R(t,0)$ at all times, in particular for $|t| \to \infty$. If $G_\sigma^R(t,0)$ decays quickly to zero, this poses no computational problem. If not, as in the interesting case close to phase transitions, very long times have to be computed, which is a hard problem due to entanglement growth in DMRG [31]. By contrast, the solution of the nonequilibrium self-consistency condition (4) does not *a priori* require us to compute very long times, as it

does not invoke a Fourier transform. Instead, one solves the self-consistency on the time domain starting at short times going successively to longer times. This makes it well suited for a DMRG treatment.

III. ENTANGLEMENT IN THE STAR VERSUS CHAIN GEOMETRY IN EQUILIBRIUM

The DMFT impurity Hamiltonian is not a physical but an effecitve model for which the only requirement is that the bath hybridization function $\Lambda(t,t')$ fulfills a DMFT self-consistency condition. Apart from this, there is no constraint, and one is, e.g., free to choose the geometry of the impurity problem. To our knowledge, up to now, for MPS/DMRG treatments of impurity problems [25–27,29–34], only the *chain* geometry has been considered, which is also used in NRG. This is due to the common belief that long-range interactions make any treament with MPS very inefficient as then *area laws* do not hold true any more. As discussed in the following, the star geometry of an impurity problem can nevertheless be highly suitable for an MPS treatment. For this analysis, we consider different SIAMs in equilibrium, as the fundamental entanglement properties of the geometry should not depend on whether Hamiltonian parameters are time dependent or not. In this section, therefore, Green's and hybridization functions are time-translationally invariant.

A. Star and chain geometry

The Hamiltonians of the SIAM in the star and the chain geometry read as

$$H^{\mathrm{star}} = H_{\mathrm{imp}} + H_{\mathrm{bath}} + H_{\mathrm{hyb}}, \tag{18a}$$

$$H_{\mathrm{imp}} = U\left(n_{0\uparrow} - \frac{1}{2}\right)\left(n_{0\downarrow} - \frac{1}{2}\right), \tag{18b}$$

$$H_{\mathrm{bath}} = \sum_{l=1}^{L_b} \sum_\sigma \epsilon_l c_{l\sigma}^\dagger c_{l\sigma}, \tag{18c}$$

$$H_{\mathrm{hyb}} = \sum_{l=1}^{L_b} \sum_\sigma \left(V_l c_{0\sigma}^\dagger c_{l\sigma} + \mathrm{H.c.}\right), \tag{18d}$$

$$H^{\mathrm{chain}} = H_{\mathrm{imp}} + H_{\mathrm{pot}} + H_{\mathrm{kin}}, \tag{18e}$$

$$H_{\mathrm{pot}} = \sum_{l=1}^{L_b} \sum_\sigma \widetilde{\epsilon}_l c_{l\sigma}^\dagger c_{l\sigma}, \tag{18f}$$

$$H_{\mathrm{kin}} = \sum_{l=0}^{L_b-1} \sum_\sigma \left(\widetilde{V}_l c_{l+1,\sigma}^\dagger c_{l\sigma} + \mathrm{H.c.}\right). \tag{18g}$$

H^{star} is a time-independent version of the representation of the SIAM chosen in the previous section in Eq. (5). The relation of both H^{star} and H^{chain} is a unitary transformation [31,35,36] defined as the matrix of Lanzcos vectors that tridiagonalizes H^{star} (and hence maps it on a chain) as recapitulated in Appendix A 2.

The hybridization functions of the SIAM in both geometries in their dependence on the Hamiltonian parameters of Eq. (18)
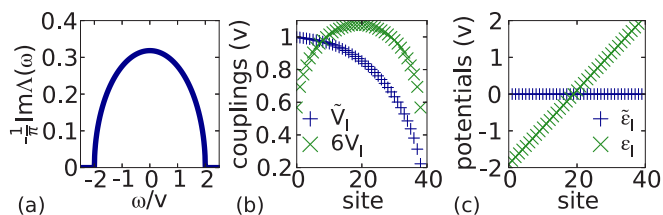
FIG. 1. (Color online) (a) Semielliptic bath spectral function $-\frac{1}{\pi}\mathrm{Im}\Lambda(\omega)$ defined in Eq. (20). (b) Corresponding couplings in the chain ($\widetilde{V}_l$) and the star (V_l) geometry. (c) Corresponding potentials in the chain ($\widetilde{\epsilon}_l$) and the star (ϵ_l) geometry. Parameters are given in units of the hopping v.

are

$$\Lambda^{\mathrm{star}}(\omega) = \sum_{l=1}^{L_b} \frac{|V_l|^2}{\omega - \epsilon_l},$$

$$\Lambda^{\mathrm{chain}}(\omega) = \cfrac{|\widetilde{V}_0|^2}{\omega - \widetilde{\epsilon}_1 - \cfrac{|\widetilde{V}_1|^2}{\omega - \widetilde{\epsilon}_2 - \cfrac{\cdots}{\omega - \widetilde{\epsilon}_{L_b-1} - \cfrac{|\widetilde{V}_{L_b-1}|^2}{\omega - \epsilon_{L_b}}}}},$$

(19)

where the first line has already been given in Eq. (17).

Consider now the example of a SIAM with a semielliptic bath spectral function, which is given by the imaginary part of the hybridization function $\Lambda(\omega + i0^+)$, where here $\omega \in \mathbb{R}$,

$$-\frac{1}{\pi}\mathrm{Im}\Lambda(\omega + i0^+) = \frac{1}{2v\pi}\sqrt{4 - \left(\frac{\omega}{v}\right)^2} \qquad (20)$$

and shown in Fig. 1(a). In the following, we will omit to specfiy the infinitesimal shift $i0^+$. To find the parameters of the SIAMs that generate this hybridization function via Eq. (19), one discretizes $-\frac{1}{\pi}\mathrm{Im}\Lambda(\omega)$ in a procedure well known from NRG, which is briefly summarized in Appendix A 1 [31,35]. The potentials ϵ_l in the star can therefore be associated with excitations of particles in different energy intervals of the bath spectral function $-\frac{1}{\pi}\mathrm{Im}\Lambda(\omega)$, but have no simple interpretation in the chain geometry. The resulting parameters are shown in Figs. 1(b) and 1(c).

We impose an order on the indices of the star bath states by sorting them according to their potential energy in ascending order [Fig. 1(c)], which maps the star on an *auxiliary chain* which should not be confused with the *chain geometry* introduced before. The decisive difference between the *auxiliary chain* and the *chain geometry* is that the former has long-range interactions while the latter has short-range interactions. We compare the case of the *chain geometry* (i) with two different maps to generate the *auxiliary chain*: (ii) placing the impurity site at the center, and (iii) placing the impurity at the first site. The *auxiliary chain* obtained in case (iii) has long-range interactions at double the range of those that occur in case (ii). One might expect this to lead to very different entanglement properties. All three cases are sketched in Fig. 2.

B. Ground-state properties

Figure 3(a) shows the density distribution in the ground state for the three setups (i)–(iii). In the star geometry, i.e., its
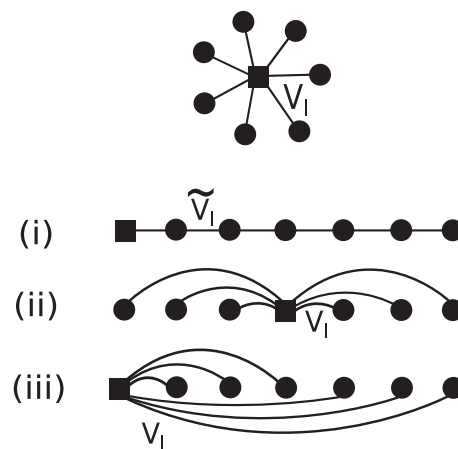

FIG. 2. Sketch of the three setups studied. The star geometry can be mapped with the unitary transform U to the *chain* geometry (i). It can also be mapped to an *auxiliary* chain by sorting the indices ascendingly to their potential energy. If one places the impurity in the center of this chain, one obtains the layout (ii), if one places it on the left edge of the chain, layout (iii) is obtained. Layouts (ii) and (iii) differ by the range over which the couplings V_l couple different lattice sites.

auxiliary chain representations (ii) and (iii), the density distribution resembles the Fermi function, where sites with negative potential energy are occupied and sites with positive energies are unoccupied. By contrast, the homogeneous potential energies of the chain geometry lead to a homogeneous density
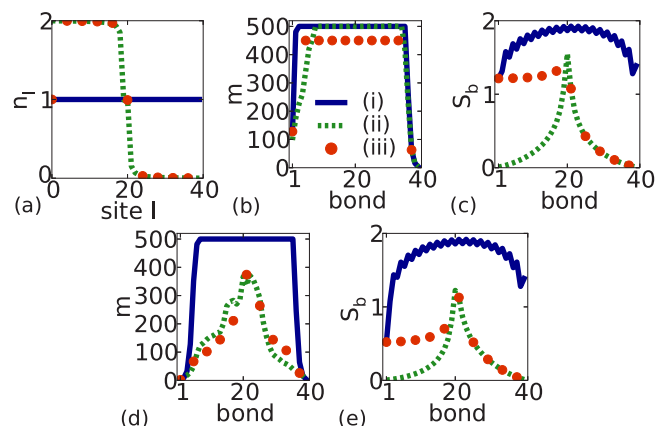

FIG. 3. (Color online) (a)–(c) Properties of the MPS approximation $|E_0\rangle$ of the ground state of a SIAM in the chain (full blue lines) in the three setups sketched in Fig. 2: (i) chain geometry (full blue lines), (ii) and (iii) star geometries with central and edge impurity (dashed green lines and red dotted lines). This is for the semielliptic bath spectral function (20) shown in Fig. 1(a) and for $U/v = 4$. (d), (e) Properties of the initial state $c_{0\sigma}^{\dagger}|E_0\rangle$ for the time evolution needed to compute the retarded Green's function. (a) Density distribution n_l. (b), (d) Bond dimension m. (c), (e) Bond entanglement entropy S_b. $L_b = 39$ sites are used to approximate the bath. The total chain length is $L = L_b + 1 = 40$. Ground states have been computed with a maximum bond dimension of $m = 500$. In the case of the chain geometry (i) this sufficed to reach a variance of $\langle [(H^{\mathrm{chain}} - E_0)/v]^2 \rangle \sim 10^{-4}$, whereas in the case of the star geometry, (ii) and (iii), one could reach $\langle [(H^{\mathrm{star}} - E_0)/v]^2 \rangle \sim 10^{-6}$. Here, E_0 denotes the numerical value of the ground-state energy.

distribution. Whereas the wave functions of electrons, which are noninteracting on all but one site of the system, is localized in the strongly inhomogeneous occupied regions in the star geometry, they are completely delocalized in the case of the chain geometry. Localization leads to low entanglement [37] and low bond dimensions, whereas delocalization leads to high entanglement. A similar observation can be made when comparing the momentum representation of free fermions, which is not entangled, with the real-space representation, which is highly entangled. The fact that locality of the ground state in the star geometry transforms to nonlocality in the chain geometry is also obvious from inspection of the concrete unitary transform, which is *not* a Fourier transform, but still associates a superposition of all star bath states with a single chain bath state [see, e.g., Eq. (A2) in Appendix A 2]. *Locality* is therefore not related to the range of interactions in this case. We note that recent progress in exact diagonalization techniques also points out the fact that efficient bath geometries should be designed in a way that avoids partially filled bath geometries [38].

Figures 3(b) and 3(c) show the bond dimensions m in the ground state and the bond entanglement entropies S_b. These support the previous conceptual arguments when taking into account that, in the case of the chain geometry (i), a maximum of $m = 500$ kept states sufficed to reach a variance of $\langle [(H^{\text{chain}} - E_0)/v]^2 \rangle \sim 10^{-4}$, whereas in the case of the star geometry (ii) and (iii), one could reach the much better value of $\langle [(H^{\text{star}} - E_0)/v]^2 \rangle \sim 10^{-6}$.

C. Time evolution

To understand how entanglement grows during time evolution, consider the computation of the *greater* Green's function for the impurity [compare its definition Eq. (11a)]

$$G_\sigma^>(t,t') = -i \langle c_{0\sigma}(t) c_{0\sigma}^\dagger(t') \rangle, \qquad (21)$$

where the expectation value at $T = 0$ is taken in the ground state. In equilibrium, where $G_\sigma^>(t,t') = G_\sigma^>(t - t')$, one can without loss of generality set $t' = 0$ and instead compute

$$G_\sigma^>(t) = -i \langle E_0 | c_{0\sigma} e^{-i(H-E_0)t} c_{0\sigma}^\dagger | E_0 \rangle. \qquad (22)$$

1. Initial state

Applying the creation operator $c_{0\sigma}^\dagger$ to the ground state destroys much of its entanglement, as can be seen by inspecting Figs. 3(d) and 3(e), which show bond dimensions and entanglement in the initial state $c_{0\sigma}^\dagger | E_0 \rangle$ used for the time evolution in Eq. (22). The action of $c_{0\sigma}^\dagger$ on the ground state $| E_0 \rangle$ cancels *exactly* all superpositions of Fock states in which the impurity site is occupied, which strongly reduces entanglement. As the impurity site is involved in almost all states in the star geometry, the action $c_{0\sigma}^\dagger$ reduces entanglement in the star geometry dramatically, almost independently of whether the site is located at the center (ii) or at the edge (iii) [Fig. 3(d)]. In the chain geometry, the site does not have such a prominent role and, therefore, reduction of entanglement is much less pronounced [Fig. 3(d)].

2. Entanglement growth

During the real-time evolution needed to compute Eq. (22), we compute each time step $\Delta t = 0.05/v$ with a precision of

$$\epsilon_{\text{err}} = || \, |\psi(t + \Delta t)\rangle - \exp(-i H \Delta t)|\psi(t)\rangle \, || < 10^{-6}, \qquad (23)$$

and do not limit the growth of bond dimensions needed to guarantee this error. Truncating the initial state down to this precision reduces the original bond dimensions shown in Fig. 3(d) to very small values. These can be seen in the short-time regions of Figs. 4(a)–4(c), where we plot the bond dimensions that occur in the three setups (i), (ii), and (iii), respectively.

In the chain geometry, the growth of the bond dimension m [Fig. 4 (a)] and of the entanglement entropy S_b [Fig. 4 (d)] is associated with the particle that is created at site 0 at time $t = 0$ and subsequently travels across the chain as seen by its density evolution shown in Fig. 4(g). In the regions that have not yet been reached by the particle, almost no change in m and S_b is observed. In the star geometry, by contrast, the particle remains almost localized [Fig. 4(h)] and entropy grows much more locally [Figs. 4(e) and 4(f)]. m_b and S_b are peaked at the center of the system as entanglement builds up only with low-energy states during time evolution. These
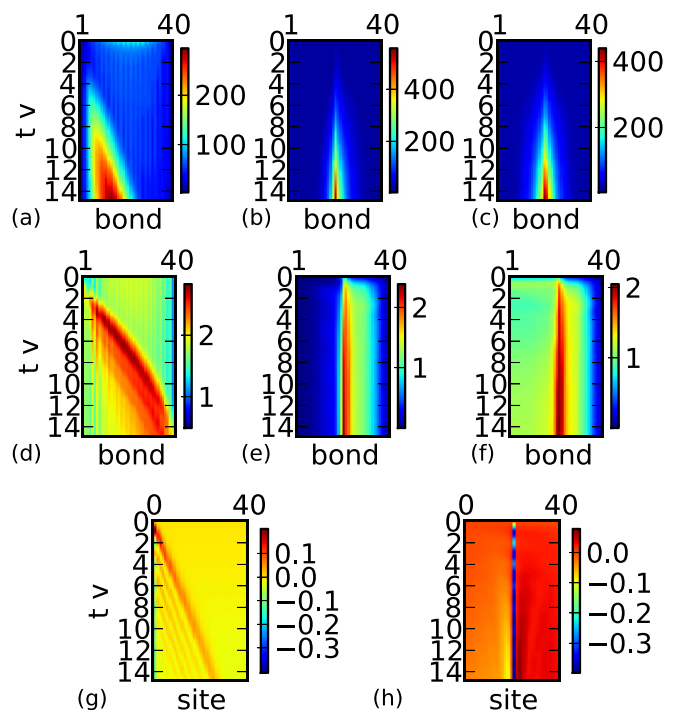

FIG. 4. (Color online) Time evolution of a SIAM with semielliptic bath spectral function (20) at $U/v = 4$ for the three setups (i)–(iii) shown in Fig. 2. The properties of the initial states for the evolution are shown in Fig. 3. Panels (a), (d), and (g) refer to the chain geometry (i), panels (b), (e), and (h) refer to the star geometry with the impurity located at the center (ii), and panels (c) and (f) to the star geometry with the impurity located at the left edge (iii). Panels (a), (b), and (c) show the local bond dimension m plotted versus bond and time, panels (d), (e), and (f) show the bond entanglement entropy S_b, and panels (g) and (h) show the density distribution substracted from its initial value $n_l(t) - n_l(0)$ plotted versus site l and time.
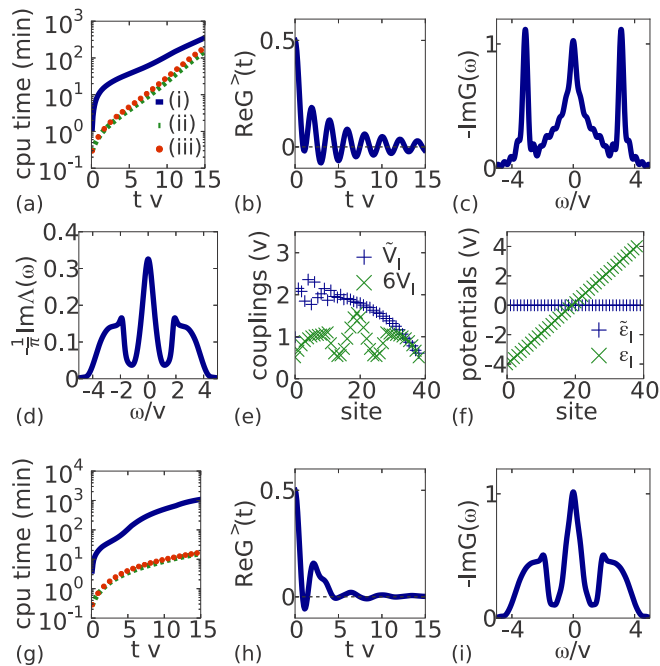
FIG. 5. (Color online) Panels (a)–(c) refer to the computation with semiellipitic bath spectral function [Fig. 1(a)]. Panels (d)–(h) refer to a computation with the self-consistently determined bath spectral function (d) for $U/v = 4$. Panels (a) and (g) show computation time versus physical time. Therein, the blue solid line refers to the chain geometry (i) whereas the green [red] dashed [dotted] line refers to the star geometry with the impurity located at the center (ii) [at the edge (iii)]. Panels (b) and (h) show the time evolution of the greater Green's function and panels (c) and (i) show the Fourier transform of the Green's function, which is the same for all three setups (i)–(iii), and therefore only one curve is shown. The oscillations in the resolution of $-\mathrm{Im}G(\omega)$ in panel (c) can be removed by convolution with a Gaussian or a Lorentzian of small width η. On the (real-) time domain, this would correspond to a slight damping (*windowing*) of $G^>(t)$ with a Gaussian or Lorentzian of large width $1/\eta$ and maximum at $t = 0$. This suppresses contributions for times $t \gtrsim 1/\eta$. Alternatively, one can compute the real-time evolution of the Green's function up to higher times, until it has converged to zero, or use an extrapolation technique such as *linear prediction* [32,39–41].

low-energy bath states are located at the center of the system irrespective of whether the impurity is located there (ii) or at the edge (iii). The buildup of entanglement with high-energy bath states would involve the occupation of these states, which is energetically strongly suppressed.

Figure 5(a) then shows how this affects the computer time needed to reach a certain physical time. The chain geometry (i) is clearly less efficient than the star geometry setups (ii) and (iii). Figures 5(b) and 5(c) show the time evolution of the Green's function and its Fourier transform, which are identical in all three setups (i)–(iii). All of the preceding results are not specific for the SIAM with semielliptic bath spectral function at $U/v = 4$. In all other cases studied by us, they are valid to an even greater extent. Consider the case with a bath spectral function $-\frac{1}{\pi}\mathrm{Im}\Lambda(\omega)$ that is the solution of the DMFT for the Bethe lattice for $U/v = 4$ as shown in Fig. 5(d). The qualitative form of the Hamiltonian parameters,
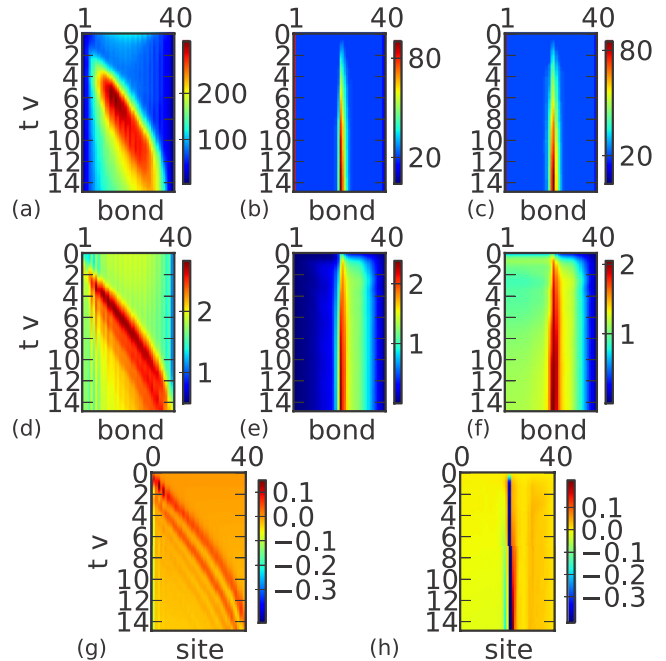

FIG. 6. (Color online) Time evolution for SIAMs in both geometries for a SIAM with self-consistently determined bath spectral function as shown in Fig. 5(d). The definition of panels is analogous to the one of Fig. 4.

shown in Figs. 5(e) and 5(f), is still similar to the previous case (Fig. 1), but the absolute magnitude of couplings and potentials is higher as the support of the bath spectral function is now of the order of $2U = 8v$. This makes the system in the star geometry more inhomogeneous and thus more localized: entanglement between sites of very different energy is disfavored energetically, whereas no such effect occurs in the chain geometry. Therefore, one sees that all computations can be performed with tremendously increased efficiency in the star geometry, which results in computation time reductions of *two orders of magnitude* as shown in Fig. 5(g). Figure 6, which is organized in the same way as Fig. 4, shows that this speedup comes with much lower bond dimensions than in the previous case (Fig. 4).

It remains to consider different values for the interaction U. It turns out that the intermediate value $U/v = 4$ leads to the strongest entanglement growth. For low and high values of the interaction U, all preceding arguments still hold true, but entanglement growth is strongly reduced in the star geometry for two further important reasons. In the noninteracting limit $U = 0$, $c_{0\sigma}^\dagger |E_0\rangle$ is an eigenstate of H. This implies that time evolution does not affect entanglement in the state. By continuity, *close* to the noninteracting limit, only very few entanglement is generated. In the strongly interacting limit $U \gg v$, very low entanglement growth is observed for a different reason. Excitation of high-energy states, i.e., occupation of bath sites with high energy in the star geometry, has to involve hopping across the impurity, where the electron needs to pay the energy for double occupation U. For high values of U, this process is strongly suppressed, and the consequence is again much lower bond dimensions than in the intermediate case $U/v = 4$. In Appendix A 3, these

arguments are supported with numerical data for the bond dimensions (Fig. 12) for all interaction strengths.

D. Nature of long-range interactions

The preceding arguments and observations show that the long-range interactions present in the *auxiliary chain* representation of the *star* geometry do not imply that it is *a priori* less suited for the treatment with MPS than the short-range interacting *chain* geometry. One should realize that the long-range interactions in the *auxiliary chain* are *not physical* interactions as they do *not* occur among *all* sites separated by a certain interaction range. They are *artificial* interactions that occur *exclusively* between the impurity site and each single bath site. If this were not the case, the calculations using the *auxiliary chain* with the impurity at the center (ii) and the left edge (iii) of the system should lead to very different entanglement, as the second case has long-range interactions at double the distance than in the first case. But, as obvious from all examples discussed before [see, e.g., the plots for the computer time in Figs. 5(a) and 5(g)], entanglement is comparable in both setups.

The physical interpretation of the concept of entanglement entropy for these long-range interacting systems is no longer meaningful. There is no physical content in the notions *left subsystem* and *right subsystem* as in the usual line of argumentation when introducing DMRG, for instance, for the case of a Heisenberg spin chain. Still, MPS can be a meaningful representation, but should then simply be interpreted as a certain way to manage and store the coefficients of the superpositions of Fock states $|\alpha_0\alpha_1\alpha_2\ldots\rangle$ where $\alpha_i \in \{0, \uparrow, \downarrow, \uparrow\downarrow\}$ denotes the local quantum state. The corresponding MPS realizes, by computing all contractions of matrices over physical quantum numbers $\{\alpha_i\}$, the subset of all possible 4^L Fock states, whose members have significant weight in a given many-body state $|\psi\rangle$. Independent of whether the underlying Hamiltonian has long-range interactions or not, bond dimensions in a given MPS can be strongly reduced by reducing the number of Fock states with significant weights in $|\psi\rangle$. In the case of the strongly inhomogeneous problem of the star geometry, states that involve occupied sites with high potential and unoccupied sites with low potential have a very small weight. In the case of the homogeneous chain geometry, no such argument applies, and *a priori* the number of Fock states with significant weight can be much higher.

IV. SOLVING NONEQUILIBRIUM DMFT USING MPS

Having motivated the usage of the star geometry of impurity problems for MPS-based algorithms in the previous section, we will now use it to solve NEQDMFT. This point is important as a formulation of NEQDMFT in the chain geometry is highly nontrivial and has not yet been achieved, whereas its formulation in the star geometry has been worked out by Eckstein [23] and Gramsch *et al.* [14].

A. Model definition

In the following, we briefly summarize the benchmark setups studied by Gramsch *et al.* [14] and Balzer *et al.* [20] by means of exact diagonalization and multiconfiguration time-

dependent Hartree. Consider the NEQDMFT for the Hubbard model on the Bethe lattice, i.e., impose the self-consistency condition (4), for an initial preparation of the system in the atomic limit ($v = 0$). The following ramp then rapidly turns on the hopping up to a final value of $v = v_0 \equiv 1$ at time $t_1 > 0$:

$$v(t) = \begin{cases} \frac{1}{2}[1 - \cos(\omega_0 t)] & \text{for} \quad t < t_1, \omega_0 = \frac{\pi}{t_1}, \\ 1 & \text{for} \quad t \geqslant t_1. \end{cases} \quad (24)$$

Since we start from the atomic limit, there are no impurity-bath correlations in the initial state and we only need to consider the *second* bath, as discussed in Sec. II.

The hybridization function $\Lambda(t,t')$ is particle-hole symmetric and spin symmetric ($\Lambda_\uparrow = \Lambda_\downarrow = \Lambda$) in the para-magnetic phase considered here. The initial ground state of the SIAM contains an equal number of empty and doubly occupied bath sites and a singly occupied impurity. In practice, we average over two Green's functions G^α and G^β, where the impurity of system α (β) is populated initially by a single up-spin (down-spin) electron. The full Green's function is then given by

$$G_\sigma(t,t') = \frac{1}{2}\big[G^\alpha_{0\sigma}(t,t') + G^\beta_{0\sigma}(t,t')\big]. \quad (25)$$

Taking the average restores particle-hole symmetry, which is not given for G^α or G^β alone.

The self-consistency condition (4) is solved in the formulation (14) by a matrix decomposition of $-i\Lambda^<(t,t')$ into coupling parameters $V_{l\sigma}(t)$, as explained in detail by Gramsch *et al.* [14]. Knowing the coupling parameters, we compute the real-time impurity Green's functions $G^s_\sigma(t,t') = \theta_C(t,t')G^{s,>}_\sigma(t,t') + \theta_C(t',t)G^{s,<}_\sigma(t,t')$ with respect to the SIAMs $s = \alpha$ and $s = \beta$ by an MPS Krylov time-evolution algorithm

$$G^{s,>}_\sigma(t,t') = -i\big\langle\psi^s_0\big|U(0,t)c_{0\sigma}U(t,t')c^\dagger_{0\sigma}U(t',0)\big|\psi^s_0\big\rangle,$$

$$G^{s,<}_\sigma(t,t') = i\big\langle\psi^s_0\big|U(0,t')c^\dagger_{0\sigma}U(t',t)c_{0\sigma}U(t,0)\big|\psi^s_0\big\rangle, \quad (26)$$

$$U(t,t') = \mathcal{T}_t \exp\left(-i\int_{t'}^t ds\, H(s)\right),$$

where $\mathcal{T}_t$ denotes the usual time-ordering operator. For this, we use a simple middle-point approximation to evolve $|\psi\rangle$ one time step Δt further,

$$|\psi(t + \Delta t)\rangle = \exp[-iH(t + \Delta t/2)\Delta t]|\psi(t)\rangle \quad (27)$$

and interpolate the Hamiltonian, i.e., the couplings $V_{l\sigma}(t)$, with standard spline interpolation.

We compute the system's kinetic energy as $E_{\text{kin}}(t) = -i\sum_\sigma \int_C ds\, \Lambda(t,s)G_\sigma(s,t')|^<_{t=t'}$, the density $\langle n(t)\rangle = -i\sum_\sigma G^<_\sigma(t,t)$, which is a conserved quantity, and the double occupation $d(t) = \langle n_{0\uparrow}(t)n_{0\downarrow}(t)\rangle$. All of these quantities are averaged over the SIAMs α and β. The double occupation also gives access to the interaction energy $E_{\text{int}}(t) = U[d(t) - \frac{1}{4}]$ and by that allows us to compute the total energy as $E_{\text{tot}} = E_{\text{kin}} + E_{\text{int}}$.

In Sec. II B, we explained that we choose the bath potentials to be homogeneous. By this, a substantial part of the discussion of Sec. III that was based on the inhomogeneity of the star geometry does not apply to the description of the present setup. There are three arguments, that still motivate the use of the star geometry. (a) The statements about the nature of long-range interactions interactions in Sec. III D remain

still valid and are independent of whether the problem is homogeneous or not. (b) If one does not start from the atomic limit, but has to consider initial correlations in the bath, this will require the representation of the *first* bath referred to in Sec. II. This will again be inhomogeneous, and all of the results of Sec. III will again apply. (c) The formulation of the nonequilibrium problem in the chain geometry is highly nontrivial, whereas in the star geometry, computations can be carried out straightforwardly.

B. Numerical results

Figure 7(a) shows the time evolution of the double occupation $d(t)$ for an interaction energy of $U = 10$. Whereas in exact diagonalization, the maximal treatable bath size was $L_b = 14$ [20], we are able to perform computations for $L_b = 24$ in a numerically controlled way. The error measure for this is the conservation of the total energy $E_{tot}(t)$ shown in the inset of Fig. 7(b). The bath size of $L_b = 24$ allows to reach $t_{max} \sim 7/v_0$, whereas the highest reached time in the literature up to now, for the case $U/v_0 = 10$, is $t_{max} \sim 2.5/v_0$ [14]. The substantial increase of the possible simulation time is related to the reduced approximation error for the hybridization function $\max |\Lambda(t,t') - \Lambda_{Cholesky}(t,t')|$ for large bath sizes as shown in Fig. 8(a).

FIG. 8. (Color online) Solid lines refer to the $U = 10$ case, dashed lines to the $U = 4$ case. Panel (a) shows the error needed to compute one time step in the DMFT scheme of $\Delta t = 0.05/v_0$. Panel (b) shows the computation time $\max |\Lambda(t,t') - \Lambda_{Cholesky}(t,t')|$ of the hybridization function. Panel (c) shows the maximal bond dimension that occurs in set of Krylov states needed to expand $\exp[-iH(t)\Delta t]$. Panel (d) shows the average bond dimension in these states. The average dimension is much lower than the maximal dimension, which can be understood when looking at the spatially resolved bond dimensions that are shown in Figs. 4 and 6 for the equilibrium case, but are typical also for the nonequilibrium case.

In Fig. 8(b), we show the computer time needed to converge one DMFT time slice $\Delta t = 0.05/v_0$ using four DMFT iterations on a slice. The computation uses two cores, one for each SIAM $s = \{\alpha, \beta\}$. Figure 8(c) shows the maximal bond dimension that occurs in the computed states to be around $m \sim 1000$ for the largest bath in the case of $U/v_0 = 10$. The average bond dimension, shown in Fig. 8(d), is much lower, as the distribution of m is strongly inhomogeneous, similarly to the cases studied before [see e.g. Fig. 6(b)]. The storage of MPS with these bond dimensions is easily feasible. The exponentially growing computation time in Fig. 8(b) limits the accessible time scales. The shown accessed times though can still be reached comparatively easily, when realizing that computations on the t-t' grid can be trivially parallelized with a linear speedup (computations on one time slice are independent from each other). In practice, we used 16 cores to compute the time evolution for $L_b = 24$ and $U = 10$. All of the above used the $U(1) \times U(1)$ symmetry of the underlying SIAMs that are associated with particle-number conservation and the S_z total spin. A computation that uses the $U(1) \times SU(2)$ symmetry should strongly increase the computational efficiency. The maximally reachable simulation time should then be around $t_{max} \sim 8/v_0 - 9/v_0$.

Let us now study the much harder case of intermediate interaction strength $U/v_0 = 4$. Figure 9 shows results for the double occupation $d(t)$ and the kinetic and total energies for this case. Entanglement entropy grows much faster than for $U/v_0 = 10$, as mixing between occupied and empty bath orbitals is energetically less suppressed, as discussed in Sec. III C 2. This is reflected in the rapid growth of bond
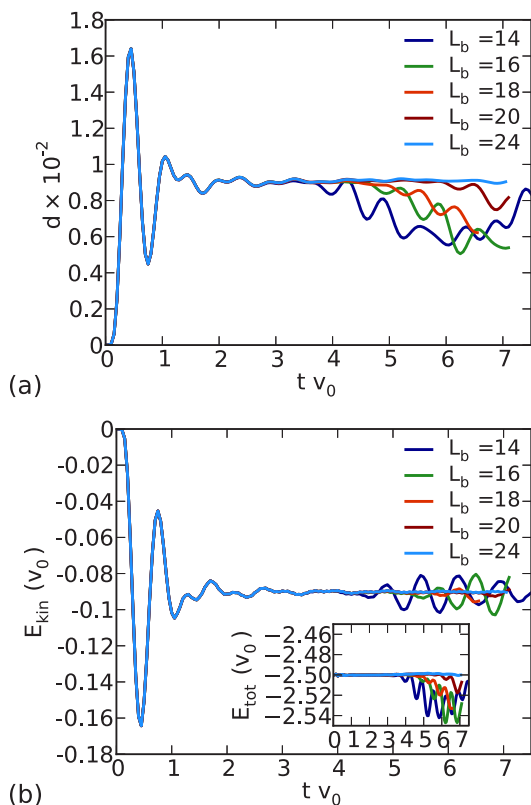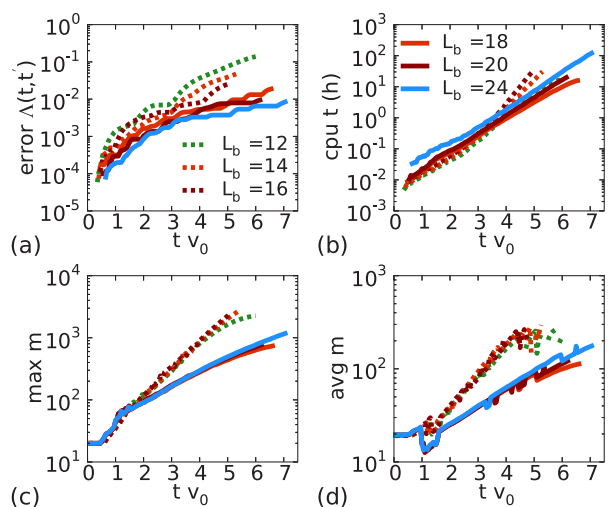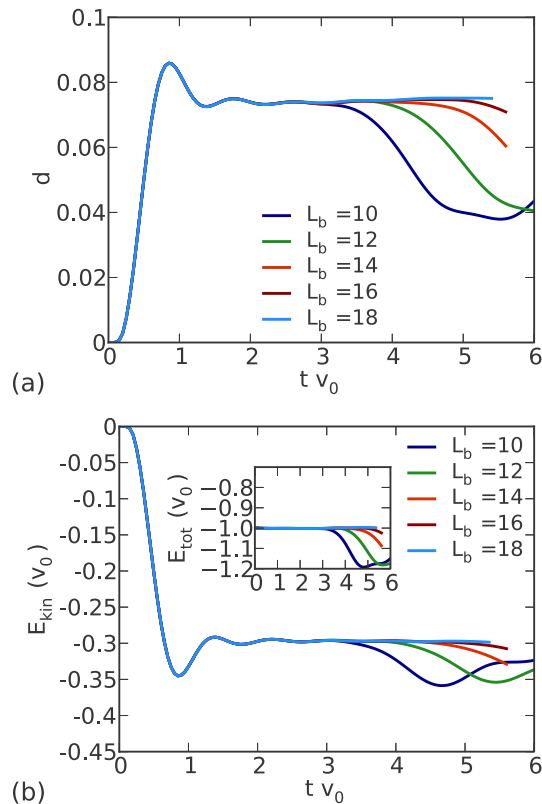

(a)

(b)

FIG. 7. (Color online) Time evolution of double occupancy $\langle d(t) \rangle$ (a) and kinetic and total energy (b) for $U = 10$ and different bath sizes. For the largest bath shown $L_b = 24$ we could reach a time $t_{max} \sim 7/v_0$ in a controlled way, meaning that the total energy is conserved. We did *not* limit the maximal allowed bond dimension m, but we imposed an upper error bound for the time evolution in single time step of $\Delta t = 0.05/v_0$ of $\epsilon_{err} = 10^{-6}$, as defined in Eq. (23).

FIG. 9. (Color online) Time evolution of double occupancy $\langle d(t) \rangle$ (a) and kinetic and total energy (b) for $U = 4$ and different bath sizes. For the largest bath shown $L_b = 18$ we could reach a time $t_{\max} \sim 5.5/v_0$ in a controlled way, meaning that the total energy is conserved.

dimensions shown by the dashed lines in Figs. 8(c) and 8(d). Still, the bath sizes treated here are beyond the regime of exact diagonalization and multiconfiguration time-dependent Hartree [20]. While Gramsch *et al.* [14] could reach $t_{\max} \sim 2.8/v_0$ using exact diagonalization, we reach $t_{\max} \sim 5.5/v_0$ by investing the computational resources shown in Fig. 8. Also here, using higher computational resources, and extrapolating the maximal bond dimension shown in Fig. 8(c), would allow us to reach $t_{\max} \sim 6/v_0$ with a maximal $m \sim 10^4$. Again, usage of the SU(2) symmetry can help to substantially increase the computational efficiency and increase the value of $t_{\max} \sim 6/v_0$.

In Appendix B, we study a simple time-dependent impurity problem as done by Balzer *et al.* [20], for which neither a self-consistency DMFT loop has to be iterated nor does time propagation need to be computed in the whole t-t' plane. This reduces computation times by orders of magnitudes, and we could reach higher values of $t_{\max}$. The entanglement growth observed for this example was comparable to the full self-consistent calculation. In Appendix C, we study an inhomogeneous reformulation of the impurity problem, motivated by the results of Sec. III C 2 that showed that strongly inhomogeneous impurity models lead to less entanglement than homogeneous models. This reformulation can be easily achieved by using the local gauge symmetry of the couplings $V_{l\sigma}(t)$, that has already been used to render the bath potentials time independent (see Sec. II B). We found, though, that

the increased driving of the system that is implied by this reformulation exactly compensates the positive effect of the inhomogeneity and, by that, the same entanglement growth is observed in both setups.

V. APPROXIMATED SELF-CONSISTENCY: RELAXATION PHASE AND STEADY PHASE

For a quench to a Hamiltonian that becomes time independent after a certain transition period, one observes that, after a *relaxation phase* that lasts until t_{relax}, the Green's function shows the time-translational invariance that it would fulfill in equilibrium $G(t,t') = G(t - t')$. Putting that differently, it fulfills the symmetry $G(t,t') = G(t + s, t' + s)$ for some intermediate time s if $\min(t,t') > t_{\mathrm{relax}}$, i.e., $G(t + s, t' + s) = \mathrm{const}(t,t')$ can be extrapolated using a constant value. By virtue of the self-consistency condition (4), the same argumentation holds true for the hybridization function, and one can conclude that, as soon as time-translational invariance is restored, one does no longer need to solve the DMFT self-consistency on the whole time slice, but already *knows* the correct $\Lambda(t,t')$ by extrapolation for times $t' > t_{\mathrm{relax}}$. The DMFT iteration needs only to be computed for "small" times on the time slice $t' \in [0, t_{\mathrm{relax}}]$, whereas usually, one has to compute it for $t' \in [0,t]$.

Figure 10(a) shows a typical self-consistently determined hybridization function $i\Lambda^>(t,t')$ for the same setup as studied in the previous section and $U = 4$. We use a bath size $L_b = 12$ here, for which the corresponding results for the double occupation have already been shown in Fig. 9(a). The symmetry $i\Lambda^>(t,t') = i\Lambda^>(t + s, t' + s)$ is obvious already from the color plot in Fig. 10(a). Figure 10(b) then studies a computation based on the extrapolated $\Lambda_{\mathrm{relax}}(t,t')$ for which the self-consistency has only been computed for times $\min(t,t') < t_{\mathrm{relax}} = 1/v_0$. As the difference to the exact computation is not perceivable with the eye, we show a color plot of the difference $i\Lambda^>_{\mathrm{relax}}(t,t') - i\Lambda^>(t,t')$. In particular for times close to the diagonal $t \sim t'$, this difference is almost zero, but also for the off-diagonal elements, it remains small.

Figure 11 shows results for the double occupation and kinetic and total energies that have been computed using the above-described approximation, and considers different values for the relaxation time t_{relax}. Already for the smallest value studied, $t_{\mathrm{relax}} = 1/v_0$, the result for the double occupation is
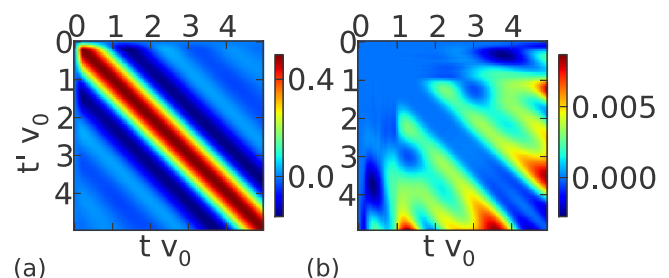

FIG. 10. (Color online) (a) Hybridization function $\Lambda(t,t')$ obtained from a calculation in which the self-consistency has been computed on the "full" t-t' grid. (b) Difference of hybridization functions $\Lambda_{\mathrm{relax}}(t,t') - \Lambda(t,t')$, where for $\Lambda_{\mathrm{relax}}(t,t')$, the self-consistency has only been solved for times $t' < t_{\mathrm{relax}} = 1/v_0$.
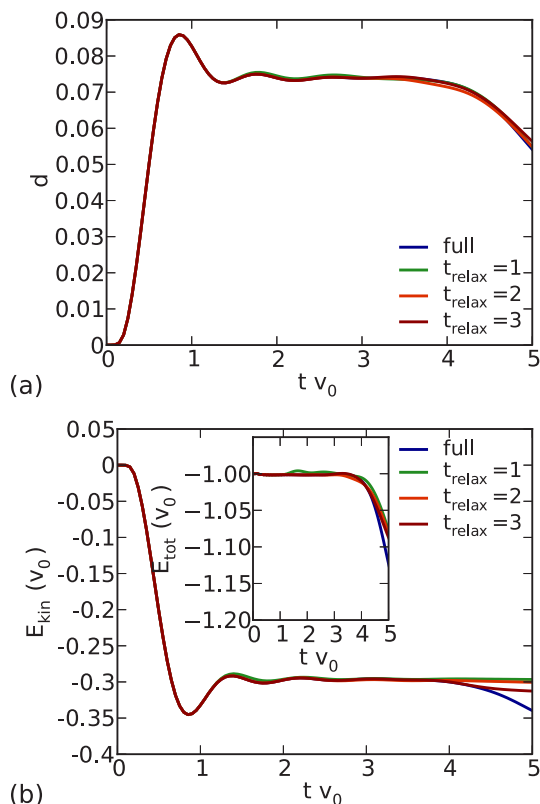
(a)

(b)

FIG. 11. (Color online) Comparison between calculation based on the approximated $\Lambda(t,t')$, for which self-consistency has only been computed for $\min(t,t') < t_{\text{relax}}$, and the exact calculation.

very close to the computation that solved the full DMFT loop. For higher values of t_{relax}, the approximation converges to the result for which the self-consistency has been solved in the full t-t' plane.

It should be interesting to study theoretically how t_{relax} depends on the initial state, quench setup, and system parameters, as it measures the time the system takes until it restores the equilibrium property of the most fundamental system parametrization, namely, the underlying $\Lambda(t,t')$, although other observables like the double occupation $d(t)$ might not yet have relaxed (compare Figs. 11 and 10). Aside from this theoretical interest, the described extrapolation scheme helps to speed up computations significantly.

The line of argumentation above should not only apply to quenches to constant Hamiltonians. Also, for periodically driven system controlled extrapolations should be possible. In this case, a constant extrapolation is no longer appropriate but, e.g., *linear prediction* can extrapolate regular oscillations with high precision [39].

VI. CONCLUSION

For equilibrium DMFT calculations, up to now, it has been difficult for DMRG/MPS-based methods to reach the computational efficiencies of CTQMC and NRG computations [25–32]. This situation should drastically be improved in view of the results of Sec. III of this paper, where we showed a tremendous speedup of more than two orders of magnitude

(Fig. 5) upon using the star instead of the chain geometry for the DMFT impurity problem. In addition to this speedup, the star geometry has tremendous technical advantages when studying impurity problems with more than two bands. While the chain representation then runs into so-called *normalization* problems for the underlyling MPS structure, this is not the case for star geometry. It now seems feasible to attack the first three-band model within DMFT using an MPS-based description.

In nonequilibrium, the situation is very different as there is no such disadvantage in computational efficiency for DMRG/MPS-based calculations. This is due to the fact that parallelization is easily feasible for the DMRG computations and one is not so much interested in the behavior of Green's functions at $t \to \infty$ (compare Sec. II C). CTQMC, by contrast, then has the *phase* problem as a big disadvantage. Although NRG has a time-dependent formulation [42], and despite recent further progress [43], it has not yet been employed to treat NEQDMFT, as is the case for the recent numerical operator method [44].

In this paper, we showed that the performance of MPS-based computations in the star geometry largely exceeds that of exact diagonalization, and bath sizes could be reached that now make it possible to study more complicated setups than quenches from the noncorrelated atomic limit.

APPENDIX A: EQUILBRIUM DMFT: COMPARISON OF STAR AND CHAIN GEOMETRIES

1. Bath discretization

The discrete approximative representation of a SIAM in the star geometry with given bath spectral function $-\frac{1}{\pi}\text{Im}\Lambda(\omega)$ is given by Hamiltonian (18a), where the parameters in H_{bath} and H_{coupl} are [31,35]

$$V_l^2 = \int_{I_l} d\omega \left[-\frac{1}{\pi}\text{Im}\Lambda(\omega) \right],$$
$$\epsilon_l = \frac{1}{V_l^2} \int_{I_l} d\omega\,\omega \left[-\frac{1}{\pi}\text{Im}\Lambda(\omega) \right]. \tag{A1}$$

Here, the bath discretization intervals are defined as $I_l = [\omega_l, \omega_{l+1}]$, and $\cup_l I_l$ should contain the support of $-\frac{1}{\pi}\text{Im}\Lambda(\omega)$. We use a linear discretization to define $\{\omega_l\}$, but a logarithmic discretization can as well be employed. The creation operators $c_{l\sigma}^\dagger$ in Eq. (18a) can be associated with excitations in a certain energy interval I_l of the bath spectral function $-\frac{1}{\pi}\text{Im}\Lambda(\omega)$.

2. Map from star to chain

Denote the bath orbital (single-particle) states of the star as $|c_l\rangle$. These are associated with the operators $c_{l\sigma}^\dagger$ in Eq. (18a) via $|c_l\rangle = c_{l\sigma}^\dagger|\text{vac}\rangle$ (we dropped the spin index in $|c_l\rangle$). The

first orbital of the chain is then defined as

$$|\widetilde{c}_1\rangle = \frac{1}{\widetilde{V}_0} \sum_{l=1}^{L_b} V_l |c_l\rangle, \quad \widetilde{V}_0 = \sqrt{\sum_l |V_l|^2}. \quad (A2)$$

It is a superposition of all states in the star. H_{hyb} in (18d) can then be written as $H_{\mathrm{hyb}} = \sum_\sigma \widetilde{V}_0(|c_{0\sigma}\rangle\langle\widetilde{c}_{1\sigma}| + \mathrm{H.c.})$. The Lanczos algorithm constructs a three-diagonal representation of $H_{\mathrm{bath}} + H_{\mathrm{hyb}}$ by representing it in its Gram-Schmidt orthogonalized Krylov basis $\{|\widetilde{c}_n\rangle\}$. H_{hyb} is already diagonal in this basis as by definition it has its single nonzero component for $\langle\widetilde{c}_1|H_{\mathrm{hyb}}|\widetilde{c}_1\rangle$, and can be ignored for the Lanczos recursion:

$$\widetilde{\epsilon}_n = \langle\widetilde{c}_n|H_{\mathrm{bath}}|\widetilde{c}_n\rangle, \quad (A3a)$$

$$|r_n\rangle = H_{\mathrm{bath}}|\widetilde{c}_n\rangle - \widetilde{\epsilon}_n|\widetilde{c}_n\rangle - \widetilde{V}_{n-1}|\widetilde{c}_{n-1}\rangle, \quad (A3b)$$

$$\widetilde{V}_n = |\langle r_n|r_n\rangle|^{\frac{1}{2}}, \quad (A3c)$$

$$|\widetilde{c}_{n+1}\rangle = \frac{1}{\widetilde{V}_n}|r_n\rangle, \quad \text{for } n = 2,\ldots,L_b - 1. \quad (A3d)$$

For $n = 1$, only the definition of $|r_n\rangle$ changes

$$|r_1\rangle = H_{\mathrm{bath}}|\widetilde{c}_1\rangle - \widetilde{\epsilon}_1|\widetilde{c}_1\rangle. \quad (A4)$$

The above equations are easily solved by multiplying from the left with $\langle c_l|$ and inserting identities $\sum_{l'} |c_{l'}\rangle\langle c_{l'}|$ such that the initial vector can be written as $(\langle c_l|\widetilde{c}_1\rangle)_{l=1}^{L_b} = (V_l)_{l=1}^{L_b}$ and the representation of H_{bath} involved is $\langle c_l|H_{\mathrm{bath}}|c_{l'}\rangle = \epsilon_l\delta_{ll'}$. Due to the numerical instability of the Lanczos algorithm, the recursion has to be computed with high-precision arithmetics.

The unitary transform that connects the two geometries via $U^\dagger(\mathcal{H}_{\mathrm{bath}} + \mathcal{H}_{\mathrm{hyb}})U = \mathcal{H}_{\mathrm{pot}} + \mathcal{H}_{\mathrm{kin}}$, where $(\mathcal{H}_{\mathrm{bath}} + \mathcal{H}_{\mathrm{hyb}})_{ll'} = \langle c_l|H_{\mathrm{bath}} + H_{\mathrm{hyb}}|c_{l'}\rangle$ and $(\mathcal{H}_{\mathrm{pot}} + \mathcal{H}_{\mathrm{kin}})_{nn'} = \langle\widetilde{c}_n|H_{\mathrm{pot}} + H_{\mathrm{kin}}|\widetilde{c}_{n'}\rangle$ is given by

$$(U)_{l,n=1}^{L_b} = ((\langle c_l|\widetilde{c}_n\rangle))_{l,n=1}^{L_b} = \begin{pmatrix} V_1/\widetilde{V}_0 & \langle c_1|\widetilde{c}_1\rangle & \ldots \\ V_2/\widetilde{V}_0 & \langle c_2|\widetilde{c}_1\rangle & \ldots \\ \vdots & \vdots & \\ V_{L_b}/\widetilde{V}_0 & & \end{pmatrix} \quad (A5)$$

and relates the two basis sets via $|\widetilde{c}_n\rangle = \sum_l U_{nl}^\dagger|c_l\rangle$.

3. Time evolution for different interaction strengths

In Fig. 12, we study the time evolution of a SIAM with semielliptic bath spectral function (20) for different interaction strengths $U/v \in \{0, 0.5, 4, 10\}$ in the chain geometry (i) and the star geometry (ii), where the detailed setups are sketched in Fig. 2. As discussed in Sec. III C 2, we observe a strongly reduced entanglement growth in the case of the star geometry in both limits of weak and strong interaction.

APPENDIX B: RESULTS FOR A NON-SELF-CONSISTENT IMPURITY PROBLEM

Here, we compute the time evolution of a SIAM with a hybridization function Λ given as

$$\Lambda(t,t') = v(t)g(t,t')v(t'), \quad t,t' \leqslant t_{\mathrm{max}} \quad (B1)$$
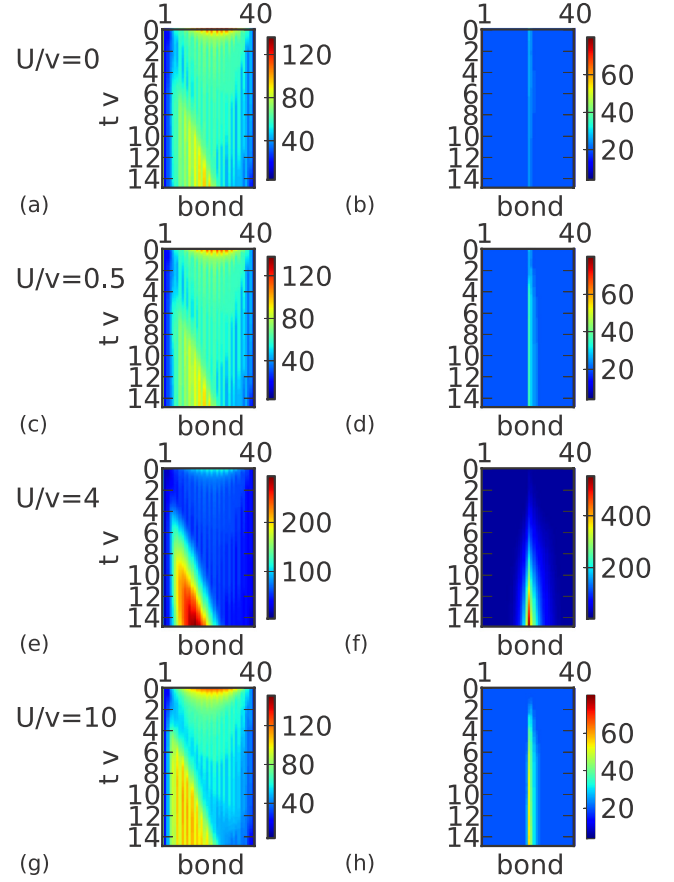

FIG. 12. (Color online) Bond dimension m versus time and bond for different interactions strengths U as given in the figure. We compare the chain geometry (i) (panels (a), (c), (e), (g)) and the star geometry with the impurity located at the center (ii) (panels (b), (d), (f), (h)). The geometries are defined in Fig. 2.

where $g(t,t') = \theta(t,t')g^>(t,t') + \theta(t',t)g^<(t,t')$ with

$$g^{\gtrless}(t,t') = \mp i \int d\omega \, f^{\gtrless}(\omega)A(\omega)e^{-i\omega(t-t')}. \quad (B2)$$

Here, $f^<(\omega) = f(\omega) = 1/(e^{\beta\omega} + 1)$, $f^>(\omega) = 1 - f(\omega)$, and the semielliptic density of states $A(\omega) = \frac{1}{2\pi}\sqrt{4 - \omega^2}$. We use the temperature $T = 1 = 1/\beta$ and the quench from the atomic limit defined in Eq. (24). This is the same setup as studied by Balzer *et al.* [20].

Figures 13(a) and 13(b) show results for the double occupation $d(t)$ obtained for two different interaction strengths $U/v_0 = 10$ and 4. For the two biggest bath sizes studied, $L_b = 20$ and 22, the value for the double occupation agrees up to times $t \sim 11/v_0$. This has been used by Balzer *et al.* [20] as indicator that the computation is controlled. But, while Balzer *et al.* [20] could only treat bath sizes up to $L_b = 16$, we are able to perform controlled computations with bath sizes up to $L_b = 24$, as has already been shown in Fig. 7, although, for the full self-consistent calculation, accessible times are much lower than here in Fig. 13. Also, we are able to efficiently treat the case $U = 4$, which is much more entangled. This limits the efficiency of multiconfiguration time-dependent Hartree as well as any MPS representation, but seems to be more severe in the former case.
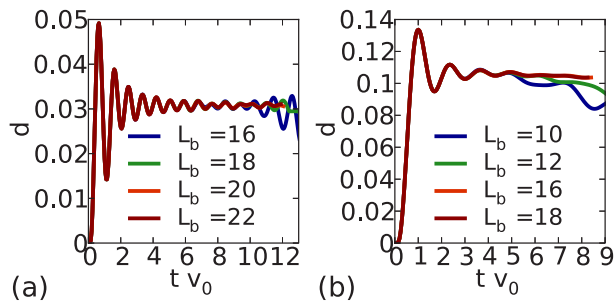
FIG. 13. (Color online) Results for the solution of the impurity model with the hybridization function defined in Eq. (B1) for two interactions $U = 10$ (a) and $U = 4$ (b). This does not involve the solution of a full self-consistent computation.
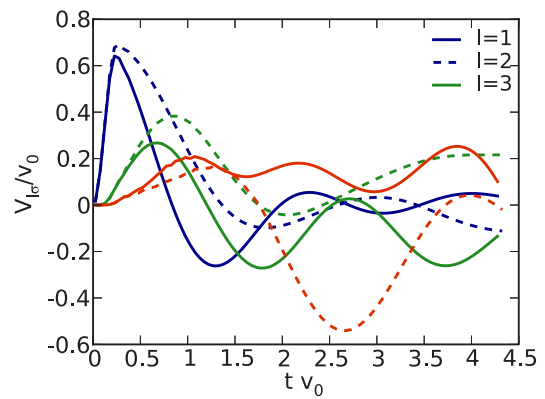

FIG. 14. (Color online) Time evolution of couplings for the case with homogeneous potential $\epsilon_{l\sigma} = 0$ (full lines) and the case with $\epsilon_{l\sigma} = -2v_0 + l4v_0/L_b$, where l runs over L_b bath sites.

APPENDIX C: REGAUGING POTENTIALS AND COUPLINGS DOES NOT INFLUENCE ENTANGLEMENT

In principle, one is free to choose the potentials of the star geometry arbitrarily if at the same time, one rescales the couplings [14]: Instead of the homogeneous star with time-independent potentials ϵ_p, which we considered in the previous sections as was done by Gramsch *et al.* [14] and Balzer *et al.* [20], one can equivalently solve an inhomogeneous star with time-independent potentials ϵ_p'. Instead of reformulating the matrix decomposition with a then oscillating noninteracting Green's function $g(t,t',\epsilon_p') \propto e^{-i\epsilon_p'(t-t')}$, one can obtain the couplings $V_p'(t)$ that correspond to the inhomogeneous

model by a simple gauge transformation of the couplings that correspond to $\epsilon_p = 0$: $V_p'(t) = V_p(t)\exp(-i\epsilon_p't)$.

We investigated the question of whether this freedom can be used to influence the entanglement properties of the system, starting from the assumption that the motion of particles in the inhomogeneous system is more constrained than in the homogeneous system. This fact is, however, compensated by the fact that the couplings $V_p'(t)$ then oscillate much slower (see Fig. 14), which leads to a stronger driving of the system. Equivalent entanglement properties result. This could have been expected, as the gauge transformation is a *local* transformation.

[1] W. Metzner and D. Vollhardt, Phys. Rev. Lett. **62**, 324 (1989).

[2] A. Georges and G. Kotliar, Phys. Rev. B **45**, 6479 (1992).

[3] A. Georges, G. Kotliar, W. Krauth, and M. J. Rozenberg, Rev. Mod. Phys. **68**, 13 (1996).

[4] G. Kotliar, S. Savrasov, K. Haule, V. Oudovenko, O. Parcollet, and C. Marianetti, Rev. Mod. Phys. **78**, 865 (2006).

[5] P. Schmidt and H. Monien, arXiv:cond-mat/0202046.

[6] J. K. Freericks, V. M. Turkowski, and V. Zlatić, Phys. Rev. Lett. **97**, 266408 (2006).

[7] H. Aoki, N. Tsuji, M. Eckstein, M. Kollar, T. Oka, and P. Werner, Rev. Mod. Phys. **86**, 779 (2014).

[8] M. Eckstein, M. Kollar, and P. Werner, Phys. Rev. Lett. **103**, 056403 (2009).

[9] M. Eckstein and P. Werner, Phys. Rev. B **82**, 115115 (2010).

[10] M. Eckstein, M. Kollar, and P. Werner, Phys. Rev. B **81**, 115131 (2010).

[11] A. Amaricci, C. Weber, M. Capone, and G. Kotliar, Phys. Rev. B **86**, 085110 (2012).

[12] N. Tsuji and P. Werner, Phys. Rev. B **88**, 165115 (2013).

[13] E. Arrigoni, M. Knap, and W. von der Linden, Phys. Rev. Lett. **110**, 086403 (2013).

[14] C. Gramsch, K. Balzer, M. Eckstein, and M. Kollar, Phys. Rev. B **88**, 235106 (2013).

[15] K. Balzer and M. Eckstein, Phys. Rev. B **89**, 035148 (2014).

[16] U. Schollwöck, Rev. Mod. Phys. **77**, 259 (2005).

[17] U. Schollwöck, Ann. Phys. (NY) **326**, 96 (2011).

[18] F. Verstraete and J. I. Cirac, arXiv:cond-mat/0407066.

[19] G. Vidal, Phys. Rev. Lett. **99**, 220405 (2007).

[20] K. Balzer, Z. Li, O. Vendrell, and M. Eckstein, arXiv:1407.6578.

[21] L. V. Keldysh, Zh. Eksp. Teor. Fiz. **47**, 1515 (1964) [Sov. Phys.– JETP **20**, 1018 (1965)].

[22] M. Eckstein, A. Hackl, S. Kehrein, M. Kollar, M. Moeckel, P. Werner, and F. A. Wolf, Eur. Phys. J. Spec. Topics **180**, 217 (2009).

[23] M. Eckstein, Ph.D. thesis, Uni Augsburg, 2009.

[24] D. J. García, K. Hallberg, and M. J. Rozenberg, Phys. Rev. Lett. **93**, 246403 (2004).

[25] S. Nishimoto and E. Jeckelmann, J. Phys.: Condens. Matter **16**, 613 (2004).

[26] S. Nishimoto, F. Gebhard, and E. Jeckelmann, J. Phys.: Condens. Matter **16**, 7063 (2004).

[27] M. Karski, C. Raas, and G. S. Uhrig, Phys. Rev. B **72**, 113110 (2005).

[28] D. J. García, E. Miranda, K. Hallberg, and M. J. Rozenberg, Phys. Rev. B **75**, 121102 (2007).

[29] M. Karski, C. Raas, and G. S. Uhrig, Phys. Rev. B **77**, 075116 (2008).

[30] M. Ganahl, P. Thunström, F. Verstraete, K. Held, and H. G. Evertz, Phys. Rev. B **90**, 045144 (2014).

[31] F. A. Wolf, I. P. McCulloch, O. Parcollet, and U. Schollwöck, Phys. Rev. B **90**, 115124 (2014).

[32] M. Ganahl, M. Aichhorn, P. Thunström, K. Held, H. G. Evertz, and F. Verstraete, arXiv:1405.6728.

[33] C. Raas, G. S. Uhrig, and F. B. Anders, Phys. Rev. B **69**, 041102 (2004).

[34] M. Nuss, M. Ganahl, E. Arrigoni, W. von der Linden, and H. G. Evertz, arXiv:1409.0646.

[35] R. Bulla, T. Costi, and T. Pruschke, Rev. Mod. Phys. **80**, 395 (2008).

[36] C. Raas, Ph.D. thesis, University of Cologne, 2005.

[37] D. Pekker and B. K. Clark, arXiv:1410.2224.

[38] Y. Lu, M. Höppner, O. Gunnarsson, and M. W. Haverkort, Phys. Rev. B **90**, 085102 (2014).

[39] W. H. Press, S. A. Teukolsky, W. T. Vetterling, and B. P. Flannery, *Numerical Recipes 3rd Edition: The Art of Scientific Computing*, 3rd ed. (Cambridge University Press, New York, 2007).

[40] S. R. White and I. Affleck, Phys. Rev. B **77**, 134437 (2008).

[41] T. Barthel, U. Schollwöck, and S. R. White, Phys. Rev. B **79**, 245101 (2009).

[42] F. B. Anders and A. Schiller, Phys. Rev. Lett. **95**, 196801 (2005).

[43] H. T. M. Nghiem and T. A. Costi, Phys. Rev. B **90**, 035129 (2014).

[44] P. Wang, G. Cohen, and S. Xu, arXiv:1410.1480.